



The Turbulent Gas Structure in the Centers of NGC 253 and the Milky Way

Nico Krieger¹, Alberto D. Bolatto², Eric W. Koch³, Adam K. Leroy⁴, Erik Rosolowsky³, Fabian Walter^{1,5}, Axel Weiß⁶, David J. Eden⁷, Rebecca C. Levy⁸, David S. Meier^{5,9}, Elisabeth A. C. Mills¹⁰, Toby Moore⁷, Jürgen Ott⁵, Yang Su¹¹, and Sylvain Veilleux²

¹ Max-Planck-Institut für Astronomie, Königstuhl 17, D-69120 Heidelberg, Germany; krieger@mpia.de

² Department of Astronomy and Joint Space-Science Institute, University of Maryland, College Park, MD 20742, USA

³ University of Alberta, Department of Physics, 4-183 CCIS, Edmonton, AB T6G 2E1, Canada

⁴ Department of Astronomy, The Ohio State University, 4055 McPherson Laboratory, 140 West 18th Avenue, Columbus, OH 43210, USA

⁵ National Radio Astronomy Observatory, P.O. Box O, 1003 Lopezville Road, Socorro, NM 87801, USA

⁶ Max-Planck-Institut für Radioastronomie, Auf dem Hügel 69, D-53121 Bonn, Germany

⁷ Astrophysics Research Institute, Liverpool John Moores University, IC2, Liverpool Science Park, 146 Brownlow Hill, Liverpool L3 5RF, UK

⁸ Department of Astronomy, University of Maryland, College Park, MD 20742, USA

⁹ New Mexico Institute of Mining and Technology, 801 Leroy Place, Socorro, NM 87801, USA

¹⁰ Department of Physics and Astronomy, University of Kansas, 1251 Wescoe Hall Drive, Lawrence, KS 66045, USA

¹¹ Purple Mountain Observatory and Key Laboratory of Radio Astronomy, Chinese Academy of Sciences, Nanjing 210034, People's Republic of China

Received 2020 February 1; revised 2020 July 14; accepted 2020 July 20; published 2020 August 26

Abstract

We compare molecular gas properties in the starbursting center of NGC 253 and the Milky Way Galactic center (GC) on scales of $\sim 1\text{--}100$ pc using dendrograms and resolution-, area-, and noise-matched data sets in CO (1–0) and CO (3–2). We find that the size–line width relations in NGC 253 and the GC have similar slope, but NGC 253 has larger line widths by factors of $\sim 2\text{--}3$. The σ^2/R dependency on column density shows that, in the GC, on scales of $10\text{--}100$ pc the kinematics of gas over $N > 3 \times 10^{21} \text{ cm}^{-2}$ are compatible with gravitationally bound structures. In NGC 253 this is only the case for column densities $N > 3 \times 10^{22} \text{ cm}^{-2}$. The increased line widths in NGC 253 originate in the lower column density gas. This high velocity dispersion, not gravitationally self-bound gas, is likely in transient structures created by the combination of high average densities and feedback in the starburst. The high densities turn the gas molecular throughout the volume of the starburst, and the injection of energy and momentum by feedback significantly increases the velocity dispersion at a given spatial scale over what is observed in the GC.

Unified Astronomy Thesaurus concepts: [Interstellar medium \(847\)](#); [Interstellar dynamics \(839\)](#); [Molecular clouds \(1072\)](#); [Starburst galaxies \(1570\)](#); [Galactic center \(565\)](#); [Stellar feedback \(1602\)](#)

Supporting material: data behind figures

1. Introduction

The interstellar medium (ISM) in the centers of spiral galaxies differs in crucial ways from that in their disks. In strongly barred galaxies, the bar helps drive gas to the galaxy center (e.g., Chown et al. 2019). This results in high gas surface densities, often organized into ring-like structures connected to the outer galaxy by dust lanes and gas streams (e.g., Buta et al. 2001; Knapen 2005; Comerón 2013; van der Laan et al. 2011; Buta 2017a, 2017b). The dynamical forces acting on the gas also differ in important ways, thanks to the deep potential well and nearly solid-body rotation often found in the centers of galaxies (e.g., Krumholz et al. 2017). As a result, the gas contents of galactic centers are typically characterized by more extreme properties than the surrounding disk: higher densities, higher temperatures, and higher velocity dispersion and turbulence (e.g., Morris & Serabyn 1996; Miyazaki & Tsuboi 2000; Oka et al. 2001; Shetty et al. 2012; Sofue 2013; Ginsburg et al. 2016; Krieger et al. 2017; Colombo et al. 2019; Mangum et al. 2019).

Not all galactic centers appear identical. Even among barred spiral galaxies, central regions vary dramatically in their gas content, star formation activity, and active galactic nucleus (AGN) activity (e.g., Kormendy & Kennicutt 2004). Because achieving high physical resolution in other galaxies is challenging, it remains an open question how the detailed ISM structure varies along with the level of activity and gas mass in the centers of galaxies. Do

more actively star-forming galaxies show increased turbulence? Do they show high surface densities at small scales?

In this paper we rigorously compare the parsec-scale molecular ISM structure between the Milky Way's relatively quiescent Galactic center (GC) and the starbursting nuclear region in NGC 253. After constructing carefully matched CO emission-line data sets, we estimate the line width–size relation and surface density for each galaxy. We compare these to one another and the expectations for self-gravitating clouds. This is the first such high-resolution, carefully matched comparison of molecular gas structure that we are aware of. Our work builds on previous studies of the GC line width–size relation by Oka et al. (2001) and Shetty et al. (2012) and a previous lower-resolution comparison of the two galaxy centers by Sakamoto et al. (2011).

In Section 2, we describe the data sets of NGC 253 and the GC. We lay out our methods, describing dendrograms and measurements, in Section 3. We show the results in Section 4, discuss them in Section 5, and summarize our work in Section 6. Appendix A lists technical details and presents checks on our methods.

1.1. The Quiescent Galactic Center

The central ~ 1 kpc of the Milky Way hosts $\approx 10\%$ of the total molecular gas mass of the Galaxy, with $\sim (6\text{--}8) \times 10^7 M_\odot$ total molecular gas mass (CMZ; Morris & Serabyn 1996; Oka et al. 1998; Ferrière et al. 2007).

Despite this high gas mass and a high fraction of dense gas, the GC is often viewed as a relatively quiescent galaxy center. The integrated star formation rate (SFR) of the GC, $\sim 0.1 M_{\odot} \text{ yr}^{-1}$, is both lower than might be expected given the amount of dense gas (e.g., Longmore et al. 2013; Barnes et al. 2017) and low compared to starbursting galaxy nuclei like NGC 253. This discrepancy has been attributed to cloud stabilization by dynamical effects or understood as catching the GC during a quiescent phase of an episodic or stochastic star formation history (e.g., Krumholz & Kruijssen 2015; Krumholz et al. 2017; Sormani & Barnes 2019). Evidence of winds and outflows from the GC hint toward more active star formation (or AGN activity) in the past (e.g., Lockman et al. 2020; Sarkar 2019).

We adopt the recent distance measurement of 8.178 kpc for the GC (Gravity Collaboration et al. 2019), for which 10 pc corresponds to $4''.2$. We refer to Sgr A* at $l, b = 359^{\circ}94422947, -0^{\circ}04615714$ as the “central position” of the GC (Petrov et al. 2011) and use 0 km s^{-1} for the systemic velocity.

1.2. The NGC 253 Starburst

The nearby galaxy NGC 253 hosts the prototypical bar-fed nuclear starburst. Its central 500 pc has an SFR $\sim 2 M_{\odot} \text{ yr}^{-1}$ and a molecular gas reservoir of $\sim (3-4) \times 10^8 M_{\odot}$ (Mauersberger et al. 1996; Leroy et al. 2015; Pérez-Beaupuits et al. 2018; Krieger et al. 2019) fueled by gas accretion along the bar (Paglione et al. 2004).

This region hosts a collection of dense, massive molecular clumps (e.g., Sakamoto et al. 2011; Ando et al. 2017) that appear to be in the process of forming super star clusters (Leroy et al. 2018). The star formation drives a wind that has been observed in H α , X-rays, and tracers of neutral and molecular gas (e.g., Turner 1985; Heckman et al. 2000; Strickland et al. 2000, 2002; Sakamoto et al. 2006; Sharp & Bland-Hawthorn 2010; Sturm et al. 2011; Westmoquette et al. 2011; Bolatto et al. 2013a; Walter et al. 2017; Krieger et al. 2019).

Despite their differences, the spatial extent and orientation of NGC 253 and the GC are quite similar. NGC 253’s inclination $i = 78^{\circ}$ compares well to the edge-on Milky Way GC. The two regions have similar size, ~ 500 pc. And the physical resolution achieved by ALMA observations of NGC 253 closely resembles that achieved by single-dish mapping in the GC.

We adopt a distance to NGC 253 of 3.5 Mpc (Rekola et al. 2005), at which 10 pc corresponds to $0''.59$. We use the kinematic center at $\alpha, \delta = 00^{\text{h}}47^{\text{m}}33^{\text{s}}.134, -25^{\circ}17^{\text{m}}19^{\text{s}}.68$ (Müller-Sánchez et al. 2010) and adopt a systemic velocity of 250 km s^{-1} .

2. Data

We aim to compare the size–line width relation, surface density, and dynamical state of the molecular gas between NGC 253 and the GC at multiple scales.

We trace the molecular gas using CO line emission, for a robust comparison requires us to compare the same tracers at the same physical resolution and sensitivity. Therefore, we construct matched CO data sets for the two galaxies, using CO (1–0) for a low-resolution comparison and CO (3–2) for a high-resolution comparison.

For NGC 253, we use ALMA CO (1–0) observations from Bolatto et al. (2013a), Leroy et al. (2015), and Meier et al. (2015) and ALMA CO (3–2) from Krieger et al. (2019). The interferometric CO (1–0) observations were carried out in ALMA

cycle 2 and then combined with Mopra single-dish observations. The final zero-spacing corrected data cube has $1''.6$ angular and 5.0 km s^{-1} spectral resolution. The CO (3–2) data were obtained with ALMA during cycle 4 and include total power observations. The resulting zero-spacing corrected data cube has $0''.15$ angular and 2.5 km s^{-1} spectral resolution. More details regarding the data reduction can be found in the original publications.

We draw CO (1–0) observations of the GC from the COGAL survey (Dame et al. 2001). These data have angular resolution $7''.5$ and spectral resolution 1.3 km s^{-1} . Note that COGAL undersamples the Galactic plane at ~ 1 beam spacing, and data have been interpolated to obtain a filled map (Dame et al. 2001). For CO (3–2), we use observations of the GC obtained by the CHIMPS2 project (D. J. Eden et al. 2020, in preparation), which extends the CHIMPS Galactic plane survey (Rigby et al. 2016) into the inner galaxy. The data build on the data reduction recipe of COHRS (CO high-resolution survey of the Galactic plane; Dempsey et al. 2013). CHIMPS2 achieves $15''.0$ spatial and 1.0 km s^{-1} spectral resolution.

We match the data between the two galaxies as closely as possible, constructing data cubes with identical spatial and spectral resolution, pixel scale, orientation with respect to the galactic plane, field of view (FOV), and noise. The following steps were followed:

- (1) The images are smoothed to circular beams with the highest possible common resolution (32 pc for CO (1–0) and 3.0 pc for CO (3–2)).
- (2) The images are then reprojected onto a common pixel grid aligned with galactic longitude and latitude. In NGC 253 we defined the galactic plane to lie along the major axis of the galaxy. We used pixel scales of 6.4 and 0.6 pc for CO (1–0) and CO (3–2), respectively, oversampling the beam by a factor of 5.
- (3) The spectral resolution is matched at 5.0 km s^{-1} for CO (1–0) and 2.5 km s^{-1} for CO (3–2). The data were reprojected onto a matched velocity grid covering from -250 to $+250 \text{ km s}^{-1}$ about the systemic velocity for both sources and both lines.
- (4) The FOV is restricted to the overlap between the images so that we study the same amount of area in each galaxy. Centered on the respective galactic center, the FOVs are 1500 pc by 750 pc for the wider FOV in CO (1–0) and 800 pc by 400 pc in CO (3–2).
- (5) After these steps, the noise in the data sets varies by a factor of ~ 2 between the NGC 253 and the GC data sets. To keep the analysis consistent between the two galaxies, we add additional beam-correlated¹² Gaussian noise to both GC images to match them to the higher noise of the NGC 253 observations. For the CHIMPS2 data, the noise varies spatially across the map and we add noise as needed to achieve a uniform noise level. The final rms noise is 38 mK in a 5.0 km s^{-1} channel in CO (1–0) and 115 mK in a 2.5 km s^{-1} channel in CO (3–2).

The final image parameters are given in Table 1.

3. Methods

We use dendrograms to identify CO-emitting structures at multiple scales and then measure their line width, luminosity,

¹² Random noise that has been convolved with a Gaussian beam and scaled to the appropriate level.

Table 1
Details of the Data Sets Used in This Analysis

Set	Source	Line	Resolution		Noise ^b (mK)	References	ALMA ID
			Spectral (km s ⁻¹)	Physical ^a (pc)			
Low	GC	CO (1–0)	5.0	32.0	38	COGAL Dame et al. (2001)	
	NGC 253	CO (1–0)	5.0	32.0	38	Bolato et al. (2013a)	2011.1.00172.S
High	GC	CO (3–2)	2.5	3.0	115	D. J. Eden et al. (2020, in preparation)	
	NGC 253	CO (3–2)	2.5	3.0	115	Krieger et al. (2019)	2015.1.00274.S

Notes.

^a FWHM of the circular beam.

^b Root mean square noise in line-free channels after matching the noise by adding beam-correlated Gaussian noise to the GC data.

and size. Using these measurements, we compare the line width and surface density between the two systems at many spatial scales.

We are particularly interested in the size–line width relation and the relationship between line width, size, and surface density, which traces the dynamical state of the gas. We then look for ways in which the different overall gas mass and level of star formation activity in the GC and NGC 253 may affect the gas structure.

3.1. Dendrogram Structure Identification

We use dendrograms to identify distinct CO-emitting structures at multiple scales. Detailed descriptions of this method are given by Rosolowsky et al. (2008), Goodman et al. (2009), and Shetty et al. (2012) and on the ASTRODENDRO homepage.¹³ Briefly, the algorithm identifies structures using a series of isointensity contours. As the contour level drops, individual discrete “leaves” identified at the highest contours merge into “branches,” which combine multiple substructures. Eventually these larger structures merge together into a “trunk,” which will not merge with any other structures. Since the structure identification is hierarchical, a given voxel in the original data cube can be included in several nested structures.

The hierarchical nature of the dendrogram approach is ideal to extract multiscale information from our high spatial dynamic range data. Recently, Li et al. (2020) tested several common clump detection algorithms and found so-called dendrograms to be among the best methods owing to high accuracy and detection completeness.

We use the ASTRODENDRO implementation, which has several tuning parameters. We only consider emission with signal-to-noise ratio > 5 (see Table 1). The minimum difference in intensity between nested structures is set to one times the rms noise. We require the minimum phase space volume per structure to be three times the spatial resolution element times the velocity channel width. The choices ensure that we focus on significant, well-resolved structures. We further restrict our analysis to the scales on which we can resolve the structures, but large-scale motions do not yet dominate the observed motions. We list these in Table 2.

3.2. Measured Quantities

The dendrograms identify $\approx 24,000$ position–position–velocity structures of interest across our data. For each structure, we measure the size, line width, and luminosity and calculate the implied mass and column density.

¹³ dendrograms.readthedocs.io

Table 2
Limits on Recoverable Structure Sizes

Source	Line	R_{\min}	R_{\max}
		(pc) (1)	(pc) (2)
NGC 253	CO (1–0)	6.0	72
GC	CO (1–0)	8.5	79
NGC 253	CO (3–2)	0.55	18
GC	CO (3–2)	0.90	20

Note. (1) Completeness limit imposed by the minimum-volume-of-a-structure threshold. (2) Limit beyond which large-scale dynamics (e.g., galactic rotation) dominate structure properties.

3.2.1. Size

We define the size, R , of a structure as the geometric mean of the semimajor and semiminor axis size. We compute these using the intensity-weighted second moment, with the major axis defined as the direction of greatest elongation of the object. This definition is implemented in ASTRODENDRO as the radius quantity.

Note that for a Gaussian cloud this definition of size corresponds to the 1σ value, while we quote beam sizes as FWHM. Also note that we do not deconvolve the beam from the structure size, trusting that our minimum-volume requirement leads us to select only well-resolved structures.

We confirm with tests that this definition of size does not affect our analyses, as other definitions merely shift the normalization of the sizes (see Appendix A.1).

3.2.2. Line Width

We define line width, σ , as the intensity-weighted second moment, i.e., the intensity-weighted velocity dispersion, over all pixels belonging to the structure. This is implemented in ASTRODENDRO as the v_{rms} quantity. Note that we do not deconvolve the channel width from the measured line widths. We also make no correction for galactic rotation or other bulk flows, which can contaminate the measurements on large scales.

Analogous to size, we confirm with tests that other definitions of line width do not affect our analyses beyond shifting the line width normalization (see Appendix A.2).

3.2.3. Luminosity

We calculate the luminosity of each structure as the area- and line-integrated intensity $L = \int I dA$, where A refers to the spatial

area and I to the line-integrated intensity $I = \int I_\nu dv$. The integrated intensity $\sum_i I_i$ is reported by ASTRODENDRO. We apply channel width and pixel area corrections to derive the luminosity.

3.2.4. Mass

From the luminosity, we estimate the molecular gas mass of each structure. For CO (1–0), we do this via $M = \alpha_{\text{CO}} L$, where α_{CO} is the CO (1–0)-to- H_2 conversion factor (see Bolatto et al. 2013b). For CO (3–2) we calculate $M = \alpha_{\text{CO}} r_{31} L$, where r_{31} is the empirical line ratio to translate from CO (3–2) to CO (1–0) luminosity.

The exact α_{CO} for galactic centers remains uncertain, though it certainly appears lower than the standard Milky Way disk value (e.g., Bolatto et al. 2013b). We adopt $\alpha_{\text{CO}} = 2.2 M_\odot \text{pc}^{-2} (\text{K km s}^{-1})^{-1}$, i.e., half the nominal solar neighborhood value, for the GC (see discussion in Kormendy & Ho 2013). We adopt a lower value $\alpha_{\text{CO}} = 1.1 M_\odot \text{pc}^{-2} (\text{K km s}^{-1})^{-1}$, i.e., one-quarter the solar neighborhood value, for NGC 253. This lower value in NGC 253 is partially motivated by observations (e.g., Leroy et al. 2015) and partially by the expectation that the denser, excited gas in NGC 253 (e.g., Mangum et al. 2019) should show starburst-like conversion factors. These numbers do not affect two of our three main results, the size–line width relation or the size–luminosity relation. The value of α_{CO} does affect the estimated dynamical state of the gas. We return to the impact of our assumption when discussing this below.

For the line ratio, we adopt $r_{31} = I_{3-2} I_{1-0}^{-1} = 0.67$ for both galaxies to keep the analysis consistent. Across each source, we measure $r_{31} = 0.63$ in NGC 253 and $r_{31} = 0.68$ in the GC after matching the area between the CO (3–2) and CO (1–0) maps. For the dendrogram structures, r_{31} may deviate from the global average and variations in r_{31} will linearly scale the CO (3–2)-based masses.

3.2.5. Column Density

We also estimate the average column density of each structure. To do this, we divide the mass by a luminosity-weighted elliptical area, A_{eff} , calculated from the major and minor axes as described above. Then, we convert to units of H_2 molecules per cm^{-2} . This column density N_{H_2} does not include helium.

3.3. Binned Analysis

The dendrogram analysis yields many structures, e.g., $>12,000$ for the CO (3–2) data of NGC 253 alone. Here we primarily focus on the average properties of structures at a given size scale or surface density. We bin the properties measured for individual structures to access these average properties. We create two sets of bins. First, we bin all structures by their size, R , in 0.1 dex wide bins. In each of these bins, we measure the median and the 16th to 84th percentile range of the line width and mass. Second, we bin the structures by surface density using bins 0.25 dex wide. In each of these bins, we measure the median and the 16th to 84th percentile range of the line width, size, and the size–line width coefficient, σ^2/R , which we use to assess the dynamical state of the gas below.

At the low end, the minimum volume of a structure limits the size measurements (R_{min} in Table 2). This limit appears as a diagonal cutoff in size–line width space. Note that the GC shows lower line width at fixed size than NGC 253; as a result,

the minimum-volume threshold imposes a higher minimum size in the GC. Also note that this effectively excludes the small structures that are most affected by beam convolution and channel convolution. Even in our smallest bins, beam deconvolution effects are $<25\%$, and because this has no effect on the analysis, we do not include any correction.

We identify the upper end of the analysis range (R_{max} in Table 2) as the size scale at which the measured line width jumps to very high values. This occurs when galactic motions dominate. The transition to this regime is sharp, making it easy to identify an upper size limit by eye.

3.4. Fitting

We conduct power-law fits to the binned data. We fit σ as a function of R (“the size–line width relation”),

$$\sigma = aR^b, \quad (1)$$

and L as a function of R (the “size–luminosity relation”),

$$L = cR^d. \quad (2)$$

To do this, we fit the bin centers and median values as lines in log–log space using a weighted least-squares minimization. We adopt the square root of the diagonals of the covariance matrix as the uncertainties, but note that these statistical errors are often small and systematic errors are nonnegligible. We discuss this more below. In addition to reporting the exponents b and d , we report the coefficients normalized to an intermediate size scale in our data, $R = 10 \text{ pc}$, $\sigma_{10 \text{ pc}}$, and $L_{10 \text{ pc}}$.

4. Results

We apply the dendrogram analysis to both lines in both galaxies. Details of the dendrogram statistics and power-law fits to the size–line width relation and size–luminosity relation are listed in Table 3. The binned data are available in the machine-readable format, and a preview is given in Table 4. In the following, we present the derived size–line width and size–luminosity relations. For each analysis, we first present data on the GC and NGC 253 followed by a comparison. In the next section, we connect these measurements via an analysis of the size–line width coefficient.

4.1. Size–Line Width Relation

Figure 1 presents the binned size–line width relations for the GC and NGC 253. With the high-resolution CO (3–2) data, we are able to cover the size range down to $<1 \text{ pc}$, whereas the lower-resolution CO (1–0) covers the larger scales up to $\sim 80 \text{ pc}$. As discussed above, we omit the largest size scales, on which we expect galactic rotation and large-scale motions to contaminate the line width.

These measurements capture the hierarchical structure of the input data. Given this, a given structure does not necessarily correspond to a (giant) molecular cloud. Especially for the CO (3–2) data, the small leaves on top of nested branches are likely not independent bound clouds, but represent substructure that could be described as “cloudlets” or “cores” within a cloud. Structures at larger scales may represent associations of multiple bound structures.

Table 3
Dendrogram Statistics and Fit Results for Power-law Fits to the Binned Size–Line Width and Size–Luminosity Relations Shown in Figures 1 and 2

Source	Line	Dendrogram Structures			Size–Line Width		Size–Luminosity	
		Total	Branches	Leaves	b (1)	$\sigma_{10\text{ pc}}$ (2)	d (3)	$\log L_{10\text{ pc}}$ (4)
NGC 253	CO (1–0)	991	466	520	0.82 ± 0.02	8.9 ± 0.2	2.92 ± 0.07	4.27 ± 0.11
GC	CO (1–0)	324	158	165	0.74 ± 0.04	3.3 ± 0.4	3.25 ± 0.13	4.34 ± 0.20
NGC 253	CO (3–2)	12414	5145	7024	0.62 ± 0.01	17.1 ± 0.1	2.89 ± 0.02	5.44 ± 0.03
GC	CO (3–2)	10235	4563	5570	0.72 ± 0.03	8.9 ± 0.2	2.69 ± 0.02	4.96 ± 0.02

Note. The errors are formal errors, which assume independent, Gaussian distributed data and underestimate the range of slopes that could be accommodated in Figures 1 and 2. (1) Exponent b of the power-law fit to the size–line width relation according to Equation (1). (2) Characteristic line width at 10 pc according to the power-law fit to the size–line width relation (Equation (1)) in km s^{-1} . (3) Exponent d of the power-law fit to the size–luminosity relation according to Equation (2). (4) Characteristic luminosity at 10 pc according to Equation (2) in $\log M_{\odot}$.

Table 4
Sample of the Binned Size–Line Width Data for CO (3–2) in NGC 253

Galaxy	CO	R_{\min} (pc) (1)	R_{\max} (pc) (2)	$\sigma_{16\text{th}}$ (km s^{-1}) (3)	σ_{median} (km s^{-1}) (4)	$\sigma_{84\text{th}}$ (km s^{-1}) (5)
NGC 253	CO (3–2)	0.49	0.62	2.24	2.87	4.10
NGC 253	CO (3–2)	0.62	0.78	2.22	3.17	4.65
NGC 253	CO (3–2)	0.78	0.98	2.53	3.71	5.66
NGC 253	CO (3–2)	0.98	1.23	3.00	4.35	6.81
NGC 253	CO (3–2)	1.23	1.55	3.35	4.99	7.86
NGC 253	CO (3–2)	1.55	1.95	3.93	5.76	9.13
NGC 253	CO (3–2)	1.95	2.46	4.42	6.69	10.73
NGC 253	CO (3–2)	2.46	3.09	4.94	7.43	11.69
NGC 253	CO (3–2)	3.09	3.89	6.24	9.31	14.06
NGC 253	CO (3–2)	3.89	4.90	7.00	10.70	16.75
NGC 253	CO (3–2)	4.90	6.17	8.14	13.33	20.37
NGC 253	CO (3–2)	6.17	7.77	9.16	11.94	23.16
NGC 253	CO (3–2)	7.77	9.78	9.42	17.68	27.99
NGC 253	CO (3–2)	9.78	12.31	12.75	21.13	26.05
NGC 253	CO (3–2)	12.31	15.50	14.00	23.03	30.71

Note. All data of the size–line width, size–luminosity, and column density– σ^2/R relations for both tracers and both sources are available in the machine-readable format in the online journal. The table shown here provides guidance regarding the form and content. (1) Lower edge of the size bin. (2) Upper edge of the size bin. (3) Lower bound of the line width distribution (16th percentile). (4) Median of the line width distribution (50th percentile). (5) Upper bound of the line width distribution (84th percentile).

4.1.1. Galactic Center

The median trend in the data is reasonably well represented by a power-law fit of the form in Equation (1), although we do measure considerable scatter about the median. The fitted slopes are $b = 0.72 \pm 0.03$ in CO (3–2) and $b = 0.74 \pm 0.04$ in CO (1–0). The typical line width at 10 pc derived from the fit is $\sigma_{10\text{ pc}} = 8.9 \pm 0.2 \text{ km s}^{-1}$ in CO (3–2) and $\sigma_{10\text{ pc}} = 3.3 \pm 0.9 \text{ km s}^{-1}$ in CO (1–0).

4.1.2. NGC 253

In NGC 253, the median of the binned CO (1–0) and CO (3–2) data (Figure 1) almost perfectly follows a power law over more than one order of magnitude. A fit results in exponents of $b = 0.62 \pm 0.01$ in CO (3–2) and $b = 0.82 \pm 0.02$ in CO (1–0). The fit yields typical line widths of $\sigma_{10\text{ pc}} = 17.1 \pm 0.1 \text{ km s}^{-1}$ in CO (3–2) and $\sigma_{10\text{ pc}} = 8.9 \pm 0.2 \text{ km s}^{-1}$ in CO (1–0).

4.1.3. Comparison of the Size–Line Width Relations

The size–line width relations in the GC and NGC 253 have similar slopes but are significantly offset in normalization.

When parameterized by Equation (1), the line widths are wider in NGC 253 by a factor of ~ 1.9 for CO (3–2) and ~ 2.7 for CO (1–0).

The GC shows a wider distribution of line widths than NGC 253 at a fixed size scale, as demonstrated by the larger vertical color bars in Figure 1. This suggests a greater variation of cloud properties in the GC compared to more uniform structures in NGC 253.

In both galaxies, the CO (3–2) line widths appear broader than the CO (1–0) line widths. At overlapping scales (8–16 pc), the CO (3–2) line widths appear ~ 1.9 times broader than CO (1–0) in NGC 253 and ~ 2.7 times broader in the GC.

The lower line widths in CO (1–0) appear to partially result from the poorer resolution of those data. As a test, we degrade the resolution of the CO (3–2) data in NGC 253 and repeat the dendrogram analysis. Degrading the spatial resolution (6.4–32 pc in 10 steps to match the CO (1–0) data) and the spectral resolution ($2.5\text{--}5.0 \text{ km s}^{-1}$) causes a shift of the size–line width relation toward larger sizes (to the right-hand side in Figure 1) that is approximately linear with resolution. At a fixed size scale, the measured line width is thus smaller with

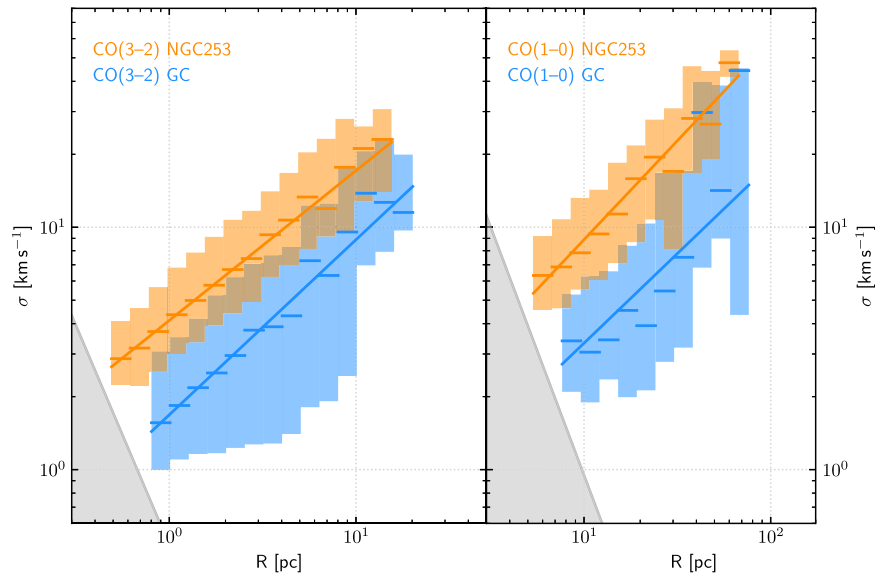


Figure 1. Binned size–line width relation for CO (3–2) (left) and CO (1–0) (right) in NGC 253 (orange) and the GC (blue). Horizontal lines indicate the median line width in each bin. The shaded colored region indicates the 16th to 84th percentile range of line widths in that size bin. The values of the power-law fits (solid lines) are given in Table 3. The gray shaded areas show regions where no structures could be detected because of our minimum-volume limit. The size–line width relation in NGC 253 is significantly offset toward larger line widths from the relation in the GC for both tracers.

(The data used to create this figure are available.)

lower-resolution data. Half of the observed line width mismatch between CO (3–2) and CO (1–0) can be explained directly as a consequence of these resolution effects.

The other half likely arises from the fact that CO (3–2) traces denser gas, usually associated with higher surface densities and more massive structures that correspondingly have larger line widths.

4.2. Size–Luminosity Relation

Figure 2 shows the size–luminosity relation, and Table 3 lists the power-law fit parameters according to Equation (2).

4.2.1. Galactic Center

The binned size–luminosity relations for CO (1–0) and CO (3–2) in the GC are well represented by power laws. The fits yield power-law exponents of $d = 2.69 \pm 0.02$ in CO (3–2) and $d = 3.25 \pm 0.13$ in CO (1–0). Given that the formal error bars understate the uncertainty, as the data are correlated across R , and if the largest bin is discarded, the CO (1–0) exponent is consistent with $d = 3$.

This is steeper than the $d = 2$ that would indicate fixed surface brightness structures, so that larger structures show higher surface brightness. The fitted slope is more similar to the $d = 3$ expected for structures with fixed volume density, assuming a constant α_{CO} . However, α_{CO} may well change as a function of luminosity or scale (e.g., as found by Solomon et al. 1987), and this will also affect the slope of the size–luminosity relation.

4.2.2. NGC 253

In NGC 253, the binned size–luminosity relations also scale nearly perfectly as power laws with exponents of $d = 2.89 \pm 0.02$ in CO (3–2) and $d = 2.92 \pm 0.07$ in CO (1–0). As in the GC, these exponents are closer to the $d \sim 3$ expected for constant

volume density and α_{CO} than the $d \sim 2$ expected for constant surface brightness.

4.2.3. Comparison of the Size–Luminosity Relation

Figure 2 shows broad similarities between the size–luminosity relations in NGC 253 and the GC. Both galaxies exhibit slopes in the range $d = 2.7$ – 3.3 for both lines. The CO (3–2) size–luminosity relations are offset by a factor of ~ 2 – 3 , with higher luminosities in NGC 253. In CO (1–0), the relations almost perfectly overlap on scales of ~ 8 – 50 pc. We do caution that this applies only to the range of plotted scales: on 1 kpc scales the CO (1–0) luminosity of the NGC 253 nucleus is 3–4 times higher than that of the GC (Jackson et al. 1996). Some of this separation is already visible in the largest-scale CO (1–0) bin.

Although the integrated line ratios are similar, more bright CO (3–2) substructure might be expected in NGC 253 compared to the GC in CO (3–2) because of the more intense ongoing star formation activity in that galaxy. Reflecting this activity, the excitation of NGC 253 has been measured to be higher (e.g., Bradford et al. 2003; Mangum et al. 2019).

As above, we emphasize that Figure 2 reflects a measurement of hierarchical structure. The plots show that dendrogram-extracted substructures with matched sizes have similar CO (1–0) luminosities in the two galaxies, not that the overall CO (1–0) distribution has the same distribution or overall luminosity in the two cases.

For reference, we also calculate the size–mass relations by applying our adopted CO-to- H_2 conversion factors (see Section 3.2.4) in Appendix B.

5. Discussion

5.1. Virial State of the Molecular Gas

Substructures in NGC 253 show higher line width at fixed size scale compared to the GC. In this section, we compare the

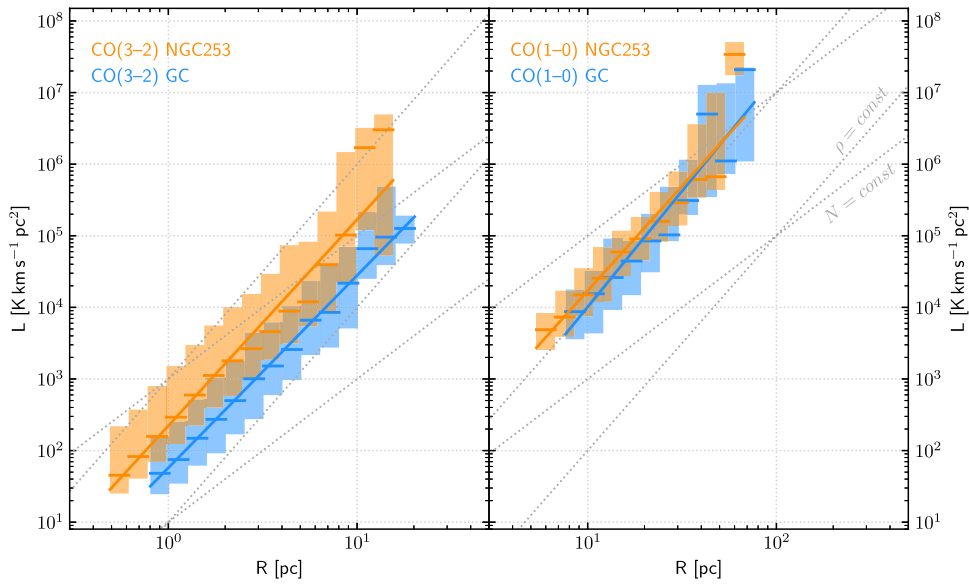


Figure 2. Relation between dendrogram structure size and luminosity for CO (3–2) (left) and CO (1–0) (right) in NGC 253 and the GC. Horizontal lines indicate the median luminosity in each bin. Shaded regions show the 16th to 84th percentile range. The values of the power-law fits (solid lines) are given in Table 3. In each panel, dotted lines illustrate two lines of constant column density N ($L \propto M \propto R^2$) and constant volume density ρ ($L \propto M \propto R^3$), calculated assuming fixed α_{CO} . (The data used to create this figure are available.)

measured line widths at fixed size to expectations for gravitationally bound clouds in virial equilibrium to explore the origins of the observed line widths.

Massive molecular clouds in the disks of the Milky Way and nearby galaxies are typically found to be close to being gravitationally bound (e.g., clouds in the Galactic disk, Solomon et al. 1987; Jackson et al. 2006; M51, Colombo et al. 2014; NGC 300, Faesi et al. 2018; and for a large recent synthetic analysis see Sun et al. 2018).

Deviation from virial equilibrium is often expressed as the virial parameter $\alpha_{\text{vir}} = 2K/U$, where K is the kinetic energy and U the gravitational potential. Following Sun et al. (2018), who follow Keto & Myers (1986) and Heyer et al. (2009), for idealized spherical clouds the line width σ , virial parameter α_{vir} , size R , and average column density N relate via

$$N = \frac{5}{f\alpha_{\text{vir}}G\pi} \frac{\sigma^2}{R}, \quad (3)$$

where G is the gravitational constant and the factor $f = (1 - \gamma/3)/(1 - 2\gamma/5)$ accounts for the internal cloud structure with a radial density profile $\rho(r) \propto r^{-\gamma}$. An isothermal cloud has $\gamma = 2$, and therefore the factor $f = 5/3$. In Equation (3), the square of the coefficient of the size–line width relation, σ^2/R , depends directly on the column density of the cloud, N . This idealized case is a vast oversimplification for real molecular clouds, but the deviation from this case can yield insight into its dynamical state and the relative contribution of gravity and forces such as external pressure or magnetic support to the measured line width.

External pressure will broaden the observed line width and increase σ^2/R . Under the assumption of virial equilibrium, the effect of external pressure on σ^2/R is described by Field et al. (2011) as

$$\frac{\sigma^2}{R} = \frac{1}{3} \left(\pi \Gamma G \Sigma + \frac{4P_e}{\Sigma} \right), \quad (4)$$

where G is the gravitational constant, Σ the mass surface density, and P_e the external pressure. Γ is a form factor of order unity (Elmegreen 1989), and we here use $\Gamma = 0.73$ for an isothermal spherical cloud of critical mass. We include the contribution of helium to the mass and derive the mass surface density $\Sigma_{\text{mol}} = 1.36 \times 2u \times N = 2.16 \times 10^{-20} N$ from the column density N in cm^{-2} to units of $M_{\odot} \text{pc}^{-2}$.

Figure 3 plots σ^2/R as a function of N for both galaxies and both lines. The dotted diagonal lines show fixed α_{vir} in the absence of external pressure, from Equation (3). The curved dashed lines show virial equilibrium for different external pressures (Equation (4)). Objects that lie far above the $\alpha_{\text{vir}} = 1$ line may either be in equilibrium with a substantial pressure exerted by an external medium or be transient and/or out of equilibrium with an excess of kinetic energy over gravitational energy. Structures that are small in size and/or low mass are, generally speaking, less likely to be in equilibrium with self-gravity (Heyer et al. 2001).

Our results in Figure 3 show a combination of both self-gravitating and high- α_{vir} substructure. Recall that the CO (1–0) data sample structures with sizes of ~ 10 – 100 pc. In the GC the structures picked out in the CO (1–0) analysis seem to approximately follow the expectations for gravitational bound objects with virial parameters $\alpha_{\text{vir}} \sim 2$ – 3 . For CO (1–0) on 10–100 pc scales in the GC, the dendrograms are consistent with those expected from self-gravity and marginally bound, $\alpha_{\text{vir}} = 2$, gas.

In the CO (1–0) measurements for the center of NGC 253 two regimes are apparent, splitting at a column density $N \sim 3 \times 10^{22} \text{ cm}^{-2}$. At lower column densities σ^2/R is approximately constant at $\sim 8 \text{ km}^2 \text{ s}^{-2} \text{ pc}^{-1}$, while for larger columns the trend appears likely to be the same as for the GC. At high column densities, our results agree with the measured line widths and dynamical state obtained by Leroy et al. (2015) studying 20–30 pc sized GMC-like structures. At lower column densities, the structures are likely either transient or in

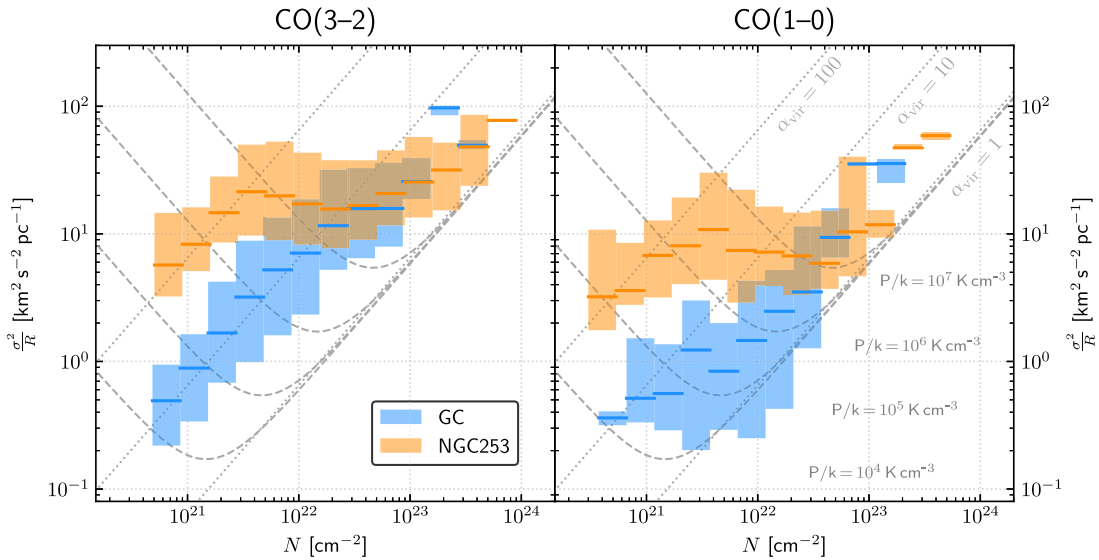


Figure 3. Size–line width coefficient as a function of column density in NGC 253 and the GC under the assumption that luminous (CO-detected) mass traces virial (gravitational) mass. Diagonal lines indicate lines of constant virial parameter under the assumption of idealized spherical clouds (see Section 5.1). Dashed lines represent lines of constant external pressure on a spherical cloud (Field et al. 2011; see Section 5.1). Horizontal lines indicate the median of the distribution of σ^2/R (colored bars) in each bin. Left: high-resolution CO (3–2); right: low-resolution CO (1–0). Note that the derived column density should be considered a lower limit (see Section 5.2). A different choice of conversion factors shifts the obtained relations along the x-axis but does not influence the slope. Due to the similar geometry and gas distribution in NGC 253 and the GC, a relative comparison is still possible even if the absolute values must be interpreted with care. The strongly enhanced σ^2/R at column densities $N \lesssim 3 \times 10^{22} \text{ cm}^{-2}$ implies that the low column density molecular gas in NGC 253 is gravitationally unbound, which is not the case in the GC. Appendix C shows this plot separated in size bins to address the degeneracy between σ and R in the size–line width coefficient.

(The data used to create this figure are available.)

equilibrium with a high external pressure. Both of these possibilities are likely, although we consider it more likely that our measurements are dominated by transient structures found by the dendrogram decomposition.

The preponderance of transient structure appears even more marked in CO (3–2), which mostly samples scales of 1–10 pc. On these smaller scales the substructures found by the dendrograms in both galaxies only appear to be self-gravitating at the largest column densities.

We know that some very massive, self-gravitating structures exist on these small scales in NGC 253; we have identified molecular clumps associated with young, massive clusters (Leroy et al. 2018). These are certainly held together by gravity, though the stars may contribute to the potential. We also know that these structures are not particularly prominent in the CO (3–2) maps (Krieger et al. 2020), which show bright CO emission throughout the starburst. Massive structures on 1–10 pc scales are also known in the GC. Several of the GMCs identified by Oka et al. (2001) in CO (1–0) have sizes $\lesssim 10$ pc. They have larger velocity dispersion for a given size than clouds in the Milky Way disk and appear to represent a population of self-gravitating clouds exposed to significant external pressure.

These massive self-gravitating structures must make up the high- N end of the left panel of Figure 3. Meanwhile, we expect that the high α_{vir} at lower column densities in CO (3–2) in both galaxies likely reflect that the dendrogram picks out substructure within larger structures, and are not by themselves bound or in equilibrium.

Both panels in both galaxies show high α_{vir} . Clouds in galaxy centers, and particularly in starbursts, are likely to have larger virial parameters than clouds in galaxy disks because of the gravity contribution from the stellar potential, the high

external pressure of the environment, the widespread presence of distributed molecular material beyond bound clouds, and the substantial amount of feedback in the form of heating and turbulence.

Synthesizing, the high line widths that we observe can be partially, but not wholly, explained by self-gravity given the estimated column densities. In both galaxies, but especially NGC 253, we see evidence that the higher column density structures have lower α_{vir} and appear more like self-gravitating structures than the structures with low column density. The low column density structures show high α_{vir} , indicating that the dendrogram picks out either transient out-of-equilibrium structures or equilibrium structures in which external pressure plays a dominant role in the dynamical state.

These observations fit with our picture of starburst galaxies. In a starburst the average density of the medium is such that most of the gas is molecular, and we expect a high optical depth molecular phase that is continuous and volume filling. Analysis of NGC 253 finds that the overall CO (1–0) luminosity is dominated by a phase with low mass-to-light ratio (relative to Milky Way disk GMCs) and average column and volume densities that are large ($N \sim 10^{23} \text{ cm}^{-2}$, $n \sim 300 \text{ cm}^{-3}$; Leroy et al. 2015). High-resolution CO (3–2) maps show the same picture, revealing pervasive high brightness line emission, even at scales of a few parsecs (Krieger et al. 2020). Embedded in this phase there are self-gravitating structures with masses $M(\text{H}_2) \sim 3 \times 10^6\text{--}10^8 M_\odot$, very large surface densities ($N \sim 4 \times 10^{23} \text{ cm}^{-2}$), and large average volume densities ($n \sim 2000 \text{ cm}^{-3}$) (Leroy et al. 2015).

Finally, we note that Figure 3 and our analysis here depend on our adopted conversion factor. We remind the reader that we adopted α_{CO} of one-half the “standard” Milky Way value for the GC and one-quarter the Milky Way value for NGC 253.

The most likely deviations from this are that the low- N gas actually has even lower α_{CO} , leading to even higher α_{vir} , while the high- N gas shows higher α_{CO} , leading to lower α_{vir} . That is, applying a more nuanced prescription would likely make the observed split between low and high column density gas even stronger.

5.2. Physical Implications

The observations discussed above can be summarized in a few key points: (1) the velocity dispersion on any given size scale in the range 1–100 pc is about 2.5 times larger in NGC 253 than in the GC. (2) The relation between luminosities and sizes is similar for NGC 253 and the GC in CO (1–0) on 8–50 pc scales, although in CO (3–2) NGC 253 is a factor of ~ 3 more luminous than the GC on scales of 1–10 pc. (3) Most structures on scales of 1–10 pc are either pressure bound or transient in both NGC 253 and the GC. (4) On scales of 10–100 pc structures in the GC appear mostly compatible with self-gravity equilibrium, while in NGC 253 this is only true for column densities over $N \sim 3 \times 10^{22} \text{ cm}^{-2}$ (equivalent to $\Sigma_{\text{mol}} \sim 500 M_{\odot} \text{ pc}^{-2}$).

These suggest that there is a widespread, highly turbulent molecular medium in the NGC 253 starburst, with higher excitation than the GC on small scales. The latter is simply a consequence of the starburst activity and is well supported by observations. For example, we know that CO excitation peaks around the $J = 7-6$ transition in NGC 253 and near the $J = 4-3$ or $5-4$ transitions in the center of the Milky Way (Bennett et al. 1994; Bradford et al. 2003). The strong departure from self-gravity for column densities lower than $N \sim 3 \times 10^{22} \text{ cm}^{-2}$, with essentially constant $\sigma^2/R \sim 7-15 \text{ km}^2 \text{ s}^{-2} \text{ pc}^{-1}$ depending on the tracer, suggests either very high pressures $P/k \sim 10^6-10^7 \text{ K cm}^{-3}$ or a medium with $\alpha_{\text{vir}} \sim 10-100$. Although the bulk gas temperatures in NGC 253 are $T \sim 50-100 \text{ K}$ (Bradford et al. 2003; Meier et al. 2015), larger than averages in the GC, the implied pressures are much in excess of plausible average thermal pressures in the system. Therefore, most of CO emission for $N \lesssim 3 \times 10^{22} \text{ cm}^{-2}$ is not tracing bound, equilibrium structures in NGC 253. It must correspond to a widespread, volume-filling molecular phase with an enhanced level of turbulence fed by the starburst activity. This phase does not have a clear correspondence in the GC.

6. Summary and Conclusion

We perform a resolution-, area-, and noise-matched comparison of molecular cloud properties in the starburst center of NGC 253 and the Milky Way GC. We compare ALMA observations of NGC 253 in CO (1–0) and CO (3–2) to data for the GC from the COGAL and CHIMPS2 surveys. Using ASTRODENDRO, we decompose the structure of the observed emission and compare the respective size–line width, size–luminosity, and σ^2/R –column density relation (related to the virial state and external pressure) over a matched range of spatial scales (approximately $R \sim 1-10 \text{ pc}$ and $R \sim 10-100 \text{ pc}$ for CO (3–2) and CO (1–0), respectively).

In the following, we briefly summarize our work and present our conclusions.

1. The size–line width relations in NGC 253 and the GC show comparable slopes, 0.7–0.8, but at any given size scale the velocity dispersion is larger in NGC 253 than the GC by a factor of ~ 2.5 .

2. NGC 253 and the GC follow similar size–luminosity relations with $L \propto R^3$, suggesting roughly constant volume density in the dendrogram-selected structures over the explored range of size scales.
3. The σ^2/R –column density relation shows that the increased line widths in NGC 253 originate in low column density gas ($N \lesssim 3 \times 10^{22} \text{ cm}^{-2}$), while at high column density ($N \gtrsim 3 \times 10^{22} \text{ cm}^{-2}$) NGC 253 and the GC occupy similar parameter space.
4. On the $R \sim 10-100 \text{ pc}$ scales sampled by the CO (1–0) emission, structures in the GC with column densities over $N \sim 3 \times 10^{21} \text{ cm}^{-2}$ show typical $\alpha_{\text{vir}} \sim 2-3$ compatible with equilibrium under self-gravity. Structures in NGC 253 are only compatible with equilibrium under self-gravity for $N \gtrsim 3 \times 10^{23} \text{ cm}^{-2}$. At lower column densities and/or on smaller spatial scales, most structures have higher α_{vir} . This implies that the low- N structures are either transient or possibly in pressure-bound virial equilibrium. Given that the bounding pressures appear implausibly high for $N \gtrsim 10^{22} \text{ cm}^{-2}$, we prefer the explanation that the dendrograms pick out transient structures at these size scales and column densities.
5. The decoupling between σ^2/R and column density observed in NGC 253 below $N \sim 10^{23} \text{ cm}^{-2}$ is likely due to a widespread molecular phase that is not bound in clouds, but that likely fills most of the volume. Such a volume-filling phase is already suggested by the pervasive high brightness emission seen in CO (3–2) maps of NGC 253 (Krieger et al. 2019). The excess kinetic energy of the unbound molecular gas in NGC 253 relative to the GC is most plausibly supplied by feedback from the starburst.

The authors would like to thank the anonymous referee for helpful comments on this work. The authors further thank Harriet Parsons for valuable feedback on the draft of this paper. This paper makes use of the following ALMA data: ADS/JAO.ALMA #2011.1.00172.S and #2015.1.00274.S. ALMA is a partnership of ESO (representing its member states), NSF (USA), and NINS (Japan), together with NRC (Canada), NSC and ASIAA (Taiwan), and KASI (Republic of Korea), in cooperation with the Republic of Chile. The Joint ALMA Observatory is operated by ESO, AUI/NRAO, and NAOJ.

The CHIMPS2 data are part of the JCMT Large Programs, with data obtained under project code M17BL004. The James Clerk Maxwell telescope is operated by the East Asian Observatory on behalf of the National Astronomical Observatory of Japan, the Academia Sinica Institute of Astronomy and Astrophysics; the Korea Astronomy and Space Science Institute, and the Center for Astronomical Mega-Science (as well as the National Key R&D Program of China with No. 2017YFA0402700). Additional funding support is provided by the Science and Technology Facilities Council of the United Kingdom and participating universities in the United Kingdom and Canada.

E.K. and E.R. acknowledge the support of the Natural Sciences and Engineering Research Council of Canada (NSERC), funding reference No. RGPIN-2017-03987. The work of A.K.L. is partially supported by the National Science Foundation (NSF) under grant Nos. 1615105, 1615109, and 1653300, as well as by the National Aeronautics and Space Administration (NASA) under ADAP grants NNX16AF48G and NNX17AF39G. E.A.C.M. gratefully

acknowledges support by the National Science Foundation under grant No. AST-1813765.

Facilities: ALMA, JCMT, CfA 1.2 m Millimeter-Wave Telescope.

Software: Astropy (Astropy Collaboration et al. 2013, 2018), Astrodendro,¹⁴ NumPy (van der Walt et al. 2011), SciPy (Jones et al. 2001), spectral-cube,¹⁵ CASA (McMullin et al. 2007).

Appendix A Definition of Structure Properties

The exact definition of size and line width of a structure can influence the derived scaling relations and inferred physical state of the gas (e.g., Ballesteros-Paredes & Mac Low 2002; Shetty et al. 2010). In this section, we explore the effect of different size and line width definitions on derived properties such as the size–line width relation.

A.1. Structure Size

The projected two-dimensional size of a structure can be defined either by its linear extent in some direction(s) or via the covered area. Using the area takes the often complex shape of structures into account but does not account for the distribution of gas within a structure. In an extreme case, 99% of the mass might be inside 1% of the area, and a good definition of structure size should come up with a size much smaller than the total extent of the cloud.

By default, ASTRODENDRO (`radius`) defines “size” as the mean structure radius of the intensity-weighted second-moment map. Mean structure radius is defined as the mean of the major axis in the direction of greatest elongation and the minor axis perpendicular to the major axis. In this comparison, we denote this definition as $R_{\text{astrodendro}}$.

We compare $R_{\text{astrodendro}}$ to two other definitions: the mean radius for an ellipse fitted to the structure, R_{ellipse} , and the mean radius of a circle with area equal to the projected structure, $R_{\text{circular}} = \sqrt{A/\pi}$, where A is the projected area of a structure.

In Figure A1 (left), we compare these three size estimates for CO (3–2) in NGC 253. The moment-based $R_{\text{astrodendro}}$ and R_{ellipse} track one another almost perfectly, modulo a small but fixed multiplicative offset related to their definitions. R_{circular} yields size a factor of ~ 2 larger because it reflects the overall footprint of the structure and not the intensity distribution. Over more than two orders of magnitude R_{circular} remains almost parallel to the other size definitions.

We use $R_{\text{astrodendro}}$, but this comparison shows that had we selected one of the other size definitions, the main effect would be to shift the normalization of the sizes.

Note that ASTRODENDRO parameterizes size as a semiaxis (instead of full axis), which allows for resolved structures apparently smaller than the spatial resolution (given as FWHM). Furthermore, this definition incorporates intensity weighting and will thus assign sizes smaller than half the resolution to structures approaching the resolution limit. The exact value depends on the distribution of emission within the structure. The minimum PPV volume threshold we chose for this analysis ensures that a structure is resolved, and derived sizes smaller than the resolution *do not* mean that a structure is unresolved. Figure A2 shows an example of a small but resolved structure in CO (3–2) in NGC 253. The size inferred by the ASTRODENDRO algorithm is 1.20 pc and thus less than half the FWHM beam size.

A.2. Structure Line Width

Similarly to size, the line width can be defined in various ways, which have different responses to the spectral and spatial distribution of emission within a structure.

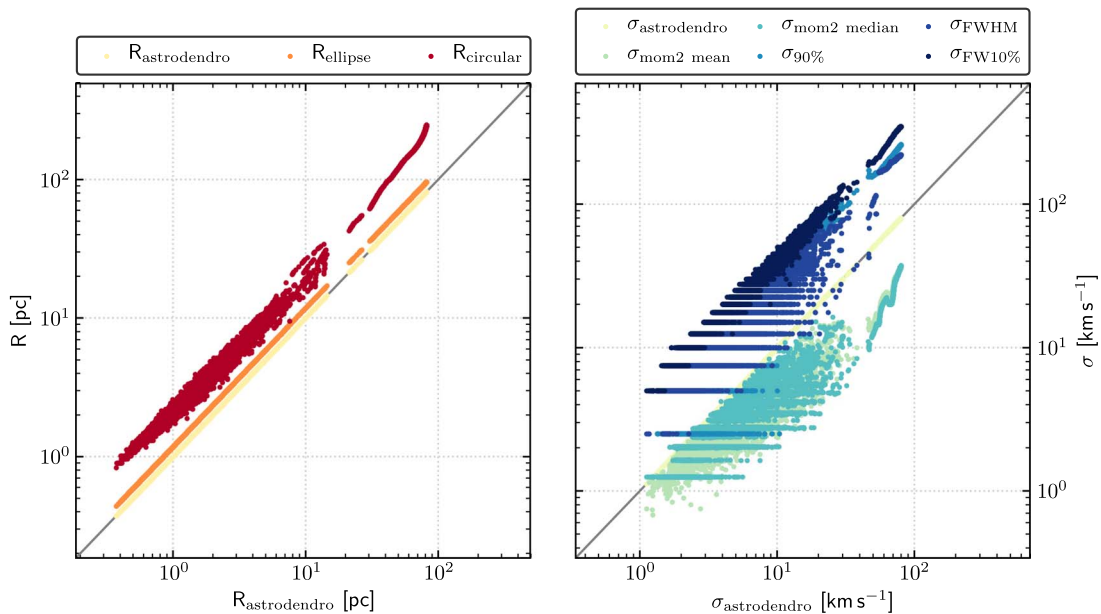


Figure A1. Comparison of different definitions for structure size (left) and line width (right). The suffix *astrodendro* refers to the quantities calculated by ASTRODENDRO directly as described in Section 3.1. For details on the other definitions for size and line width see Appendices A.1 and A.2, respectively. Quantization apparent in some line width definitions follows directly from the discrete channel structure of the data cubes.

¹⁴ dendrograms.readthedocs.io

¹⁵ <https://spectral-cube.readthedocs.io>

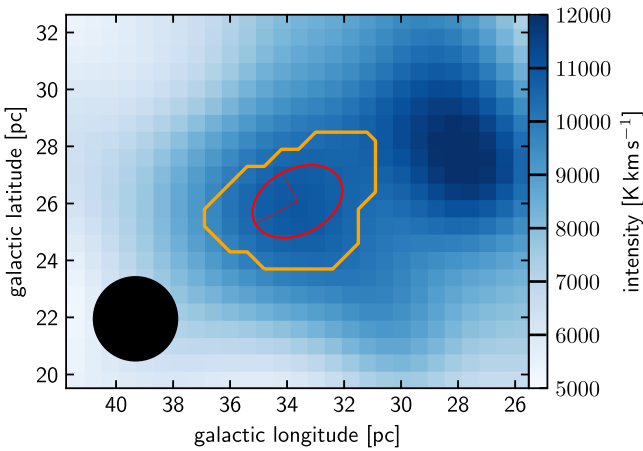


Figure A2. Example of how ASTRODENDRO assigns sizes to structures. The figure shows a random structure (#4822) in the CO (3–2) data set of NGC 253, which describes a local emission peak. The total extent of the structure (orange) and the corresponding intensity-weighted second-moment ellipse (red) are plotted on top of the total integrated intensity (zeroth-moment) CO (3–2) map (blue). Dashed lines indicate the semimajor and semiminor axes, where the mean defines the size of the structure, here $R = 1.20$ pc. The beam of 3 pc FWHM is shown in the lower left corner. Note that the background image shows all data to provide context, whereas the size ellipse is calculated for the particular structure within the orange line. In this special case of a small structure, the ASTRODENDRO algorithm assigns a size smaller than the beam to the structure. Nevertheless, the structure is resolved.

In our analysis, we use the default v_{rms} quantity in ASTRODENDRO, which we label $\sigma_{\text{astrodendro}}$ here. This quantity represents the second moment of the integrated spectrum of the structure in question. In the right panel of Figure A1, we compare this to four other line width metrics. First, $\sigma_{\text{mom2 mean}}$ and $\sigma_{\text{mom2 median}}$ represent the median and mean of the second-moment map over the footprint of the structure. These measurements effectively remove scatter in the mean velocity

from line of sight to line of sight. We also show results for σ_{90} , the line width that captures 90% of the emission in the integrated spectrum; σ_{FWHM} , the FWHM of the integrated spectrum; and σ_{10} , the width at 10% of the maximum for the integrated spectrum. Similar to the use of area above, these other line width measures are sensitive to the shape of the spectrum in different ways than the second image moment.

Note that we do not correct all of our line width measures onto a common system. That is, σ_{FWHM} is the FWHM of the line. Even for an ideal Gaussian line we expect it to differ from the rms line width by a factor of 2.354. This leads to systematic offsets in Figure A1 without any actual difference in measured line width.

Figure A1 (right) shows the comparison of these six line width definitions for CO (3–2) in NGC 253. Aside from the highest line width structures, which represent the trunks and lowest branches in the dendrogram tree, the different definitions lie approximately parallel to each other, indicating that only the normalization changes. Choosing a different definition of line width will thus not distort derived relations but merely shift them.

Appendix B Size–Mass Relation

In Figure B1, we show the size–mass relation. This figure is derived from Figure 2 by applying our adopted CO-to- H_2 conversion factors. Because we adopt α_{CO} two times smaller in NGC 253 compared to the GC, the mass–radius relations appear more similar than the size–luminosity relations. That is, NGC 253 is more luminous than the GC in CO (3–2), but our adopted conversion factor removes this difference from the mass-based relation.

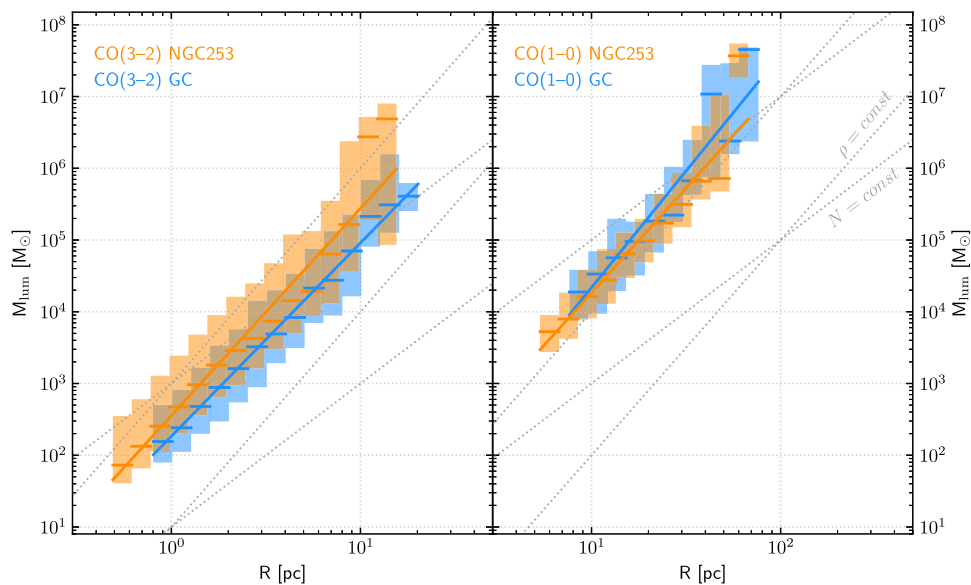


Figure B1. Relation between dendrogram structure size and mass for CO (3–2) (left) and CO (1–0) (right) in NGC 253 and the GC. Horizontal lines indicate the median of the distribution of masses (colored bars) in each bin. The power-law fits (solid lines) correspond to those to the size–luminosity relation (Table 3). The masses are derived applying our adopted conversion factors, with α_{CO} for NGC 253 two times lower than for the GC. In each panel, two lines of constant surface density ρ ($M \propto R^2$) and constant volume density N ($M \propto R^3$) are shown for reference.

Appendix C Virial State of the Gas Separated by Size Scale

The interpretation of Figure 3 is complicated by the fact that the size–line width coefficient σ^2/R is degenerate between σ

and R . In Figure C1, we keep the size fixed (up to a factor of two), so that any change in σ^2/R must be driven by σ .

Aside from the fact that there are very few bins <4 pc in CO (1–0) and >16 pc in CO (3–2), there is no relevant deviation

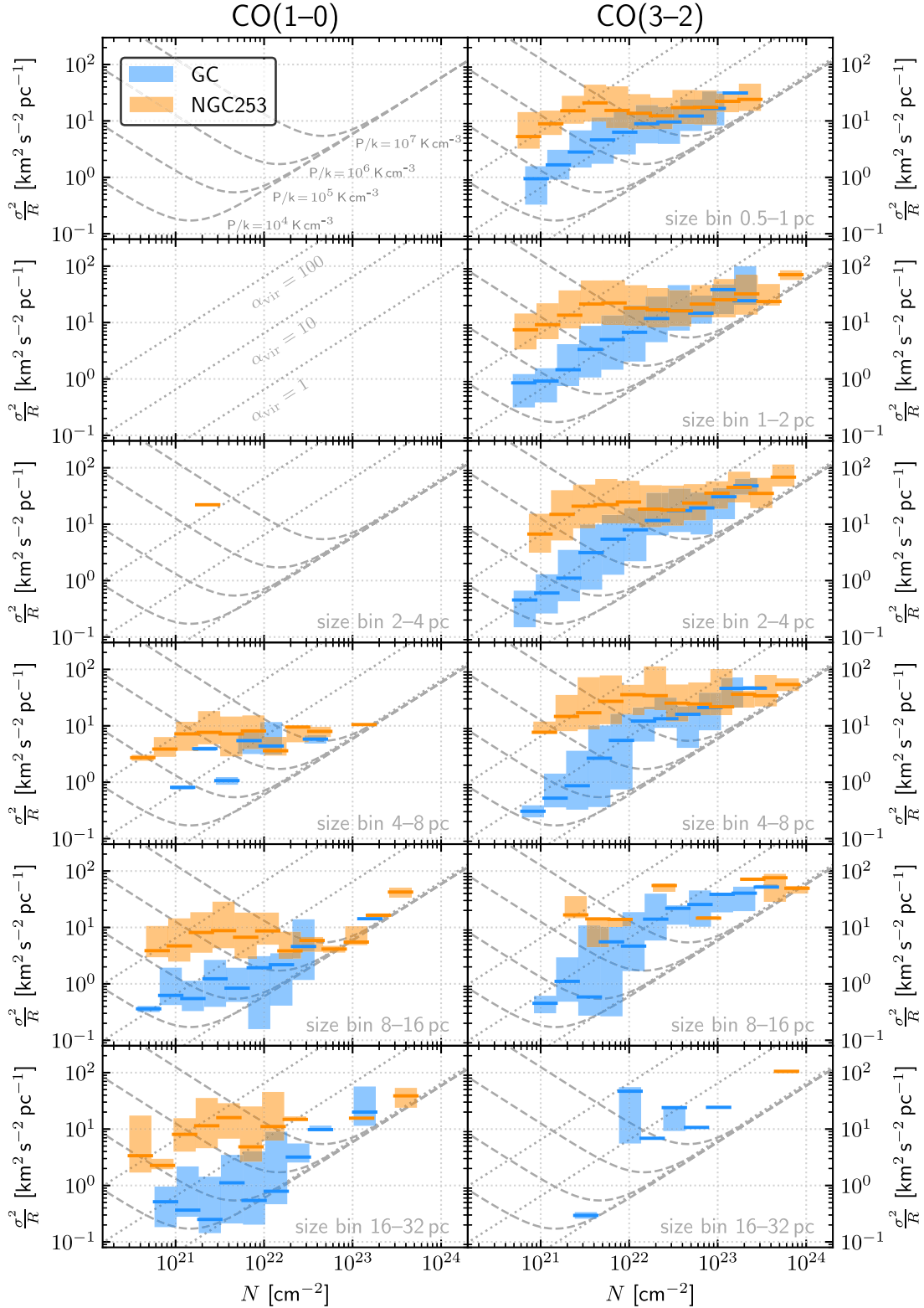




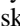


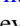

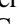




Figure C1. Size–line width coefficient σ^2/R as a function of column density for a range of structure size bins. Diagonal lines indicate lines of constant virial parameter under the assumption of idealized spherical clouds (see Section 5.1). Dashed lines represent lines of constant external pressure on a spherical cloud (see Section 5.1). Horizontal lines indicate the median of the distribution of σ^2/R (colored bars) in each bin. Left: low-resolution CO (1–0); right: high-resolution CO (3–2). The size bin for each panel is given in the lower right corner.

between the six vertical panels of Figure C1. The collapsed data as shown in Figure 3 thus capture the complete picture.

ORCID iDs

Nico Krieger  <https://orcid.org/0000-0003-1104-2014>
 Alberto D. Bolatto  <https://orcid.org/0000-0002-5480-5686>
 Eric W. Koch  <https://orcid.org/0000-0001-9605-780X>
 Adam K. Leroy  <https://orcid.org/0000-0002-2545-1700>
 Erik Rosolowsky  <https://orcid.org/0000-0002-5204-2259>
 Fabian Walter  <https://orcid.org/0000-0003-4793-7880>
 Axel Weiß  <https://orcid.org/0000-0003-4678-3939>
 Rebecca C. Levy  <https://orcid.org/0000-0003-2508-2586>
 David S. Meier  <https://orcid.org/0000-0001-9436-9471>
 Elisabeth A. C. Mills  <https://orcid.org/0000-0001-8782-1992>
 Jürgen Ott  <https://orcid.org/0000-0001-8224-1956>
 Sylvain Veilleux  <https://orcid.org/0000-0002-3158-6820>

References

- Ando, R., Nakanishi, K., Kohno, K., et al. 2017, *ApJ*, 849, 81
 Astropy Collaboration, Price-Whelan, A. M., Sipőcz, B. M., et al. 2018, *AJ*, 156, 123
 Astropy Collaboration, Robitaille, T. P., Tollerud, E. J., et al. 2013, *A&A*, 558, A33
 Ballesteros-Paredes, J., & Mac Low, M.-M. 2002, *ApJ*, 570, 734
 Barnes, A. T., Longmore, S. N., Battersby, C., et al. 2017, *MNRAS*, 469, 2263
 Bennett, C. L., Fixsen, D. J., Hinshaw, G., et al. 1994, *ApJ*, 434, 587
 Bolatto, A. D., Warren, S. R., Leroy, A. K., et al. 2013a, *Natur*, 499, 450
 Bolatto, A. D., Wolfire, M., & Leroy, A. K. 2013b, *ARA&A*, 51, 207
 Bradford, C. M., Nikola, T., Stacey, G. J., et al. 2003, *ApJ*, 586, 891
 Buta, R., Ryder, S. D., Madsen, G. J., et al. 2001, *AJ*, 121, 225
 Buta, R. J. 2017a, *MNRAS*, 471, 4027
 Buta, R. J. 2017b, *MNRAS*, 470, 3819
 Chown, R., Li, C., Athanassoula, E., et al. 2019, *MNRAS*, 484, 5192
 Colombo, D., Hughes, A., Schinnerer, E., et al. 2014, *ApJ*, 784, 3
 Colombo, D., Rosolowsky, E., Duarte-Cabral, A., et al. 2019, *MNRAS*, 483, 4291
 Comerón, S. 2013, *A&A*, 555, L4
 Dame, T. M., Hartmann, D., & Thaddeus, P. 2001, *ApJ*, 547, 792
 Dempsey, J. T., Thomas, H. S., & Currie, M. J. 2013, *ApJS*, 209, 8
 Elmegreen, B. G. 1989, *ApJ*, 338, 178
 Faesi, C. M., Lada, C. J., & Forbrich, J. 2018, *ApJ*, 857, 19
 Ferrière, K., Gillard, W., & Jean, P. 2007, *A&A*, 467, 611
 Field, G. B., Blackman, E. G., & Keto, E. R. 2011, *MNRAS*, 416, 710
 Ginsburg, A., Henkel, C., Ao, Y., et al. 2016, *A&A*, 586, A50
 Goodman, A. A., Rosolowsky, E. W., Borkin, M. A., et al. 2009, *Natur*, 457, 63
 Gravity Collaboration, Abuter, R., Amorim, A., et al. 2019, *A&A*, 625, L10
 Heckman, T. M., Lehnert, M. D., Strickland, D. K., & Armus, L. 2000, *ApJS*, 129, 493
 Heyer, M., Krawczyk, C., Duval, J., & Jackson, J. M. 2009, *ApJ*, 699, 1092
 Heyer, M. H., Carpenter, J. M., & Snell, R. L. 2001, *ApJ*, 551, 852
 Jackson, J. M., Heyer, M. H., Paglione, T. A. D., & Bolatto, A. D. 1996, *ApJL*, 456, L91
 Jackson, J. M., Rathborne, J. M., Shah, R. Y., et al. 2006, *ApJS*, 163, 145
 Jones, E., Oliphant, T., Peterson, P., et al. 2001, SciPy: Open Source Scientific Tools for Python, Web, <http://www.scipy.org/>
 Keto, E. R., & Myers, P. C. 1986, *ApJ*, 304, 466
 Knapen, J. H. 2005, *A&A*, 429, 141
 Kormendy, J., & Ho, L. C. 2013, *ARA&A*, 51, 511
 Kormendy, J., & Kennicutt, R. C. J. 2004, *ARA&A*, 42, 603
 Krieger, N., Bolatto, A. D., Leroy, A. K., et al. 2020, *ApJ*, 897, 176
 Krieger, N., Bolatto, A. D., Walter, F., et al. 2019, *ApJ*, 881, 43
 Krieger, N., Ott, J., Beuther, H., et al. 2017, *ApJ*, 850, 77
 Krumholz, M. R., & Kruijssen, J. M. D. 2015, *MNRAS*, 453, 739
 Krumholz, M. R., Kruijssen, J. M. D., & Crocker, R. M. 2017, *MNRAS*, 466, 1213
 Leroy, A. K., Bolatto, A. D., Ostriker, E. C., et al. 2015, *ApJ*, 801, 25
 Leroy, A. K., Bolatto, A. D., Ostriker, E. C., et al. 2018, *ApJ*, 869, 126
 Li, C., Wang, H.-c., Wu, Y.-w., Ma, Y.-h., & Lin, L.-h. 2020, *RAA*, 20, 031
 Lockman, F. J., di Teodoro, E. M., & McClure-Griffiths, N. M. 2020, *ApJ*, 888, 51
 Longmore, S. N., Bally, J., Testi, L., et al. 2013, *MNRAS*, 429, 987
 Mangum, J. G., Ginsburg, A. G., Henkel, C., et al. 2019, *ApJ*, 871, 170
 Mauersberger, R., Henkel, C., Wielebinski, R., Wiklind, T., & Reuter, H. P. 1996, *A&A*, 305, 421
 McMullin, J. P., Waters, B., Schiebel, D., Young, W., & Golap, K. 2007, in ASP Conf. Ser. 376, adass XVI, ed. R. A. Shaw, F. Hill, & D. J. Bell (Tucson, AZ: Univ. Arizona Press), 127
 Meier, D. S., Walter, F., Bolatto, A. D., et al. 2015, *ApJ*, 801, 63
 Miyazaki, A., & Tsuboi, M. 2000, *ApJ*, 536, 357
 Morris, M., & Serabyn, E. 1996, *ARA&A*, 34, 645
 Müller-Sánchez, F., González-Martín, O., Fernández-Ontiveros, J. A., Acosta-Pulido, J. A., & Prieto, M. A. 2010, *ApJ*, 716, 1166
 Oka, T., Hasegawa, T., Sato, F., Tsuboi, M., & Miyazaki, A. 1998, *ApJS*, 118, 455
 Oka, T., Hasegawa, T., Sato, F., et al. 2001, *ApJ*, 562, 348
 Paglione, T. A. D., Yam, O., Tosaki, T., & Jackson, J. M. 2004, *ApJ*, 611, 835
 Pérez-Beaupuits, J. P., Güsten, R., Harris, A., et al. 2018, *ApJ*, 860, 23
 Petrov, L., Kovalev, Y. Y., Fomalont, E. B., & Gordon, D. 2011, *AJ*, 142, 35
 Rekola, R., Richer, M. G., McCall, M. L., et al. 2005, *MNRAS*, 361, 330
 Rigby, A. J., Moore, T. J. T., Plume, R., et al. 2016, *MNRAS*, 456, 2885
 Rosolowsky, E. W., Pineda, J. E., Kauffmann, J., & Goodman, A. A. 2008, *ApJ*, 679, 1338
 Sakamoto, K., Ho, P. T. P., Iono, D., et al. 2006, *ApJ*, 636, 685
 Sakamoto, K., Mao, R.-Q., Matsushita, S., et al. 2011, *ApJ*, 735, 19
 Sarkar, K. C. 2019, *MNRAS*, 482, 4813
 Sharp, R. G., & Bland-Hawthorn, J. 2010, *ApJ*, 711, 818
 Shetty, R., Beaumont, C. N., Burton, M. G., Kelly, B. C., & Klessen, R. S. 2012, *MNRAS*, 425, 720
 Shetty, R., Collins, D. C., Kauffmann, J., et al. 2010, *ApJ*, 712, 1049
 Sofue, Y. 2013, *PASJ*, 65, 118
 Solomon, P. M., Rivolo, A. R., Barrett, J., & Yahil, A. 1987, *ApJ*, 319, 730
 Sormani, M. C., & Barnes, A. T. 2019, *MNRAS*, 484, 1213
 Strickland, D. K., Heckman, T. M., Weaver, K. A., & Dahlem, M. 2000, AAS Meeting, 5, 15.14
 Strickland, D. K., Heckman, T. M., Weaver, K. A., Hoopes, C. G., & Dahlem, M. 2002, *ApJ*, 568, 689
 Sturm, E., González-Alfonso, E., Veilleux, S., et al. 2011, *ApJL*, 733, L16
 Sun, J., Leroy, A. K., Schrubba, A., et al. 2018, *ApJ*, 860, 172
 Turner, B. E. 1985, *ApJ*, 299, 312
 van der Laan, T. P. R., Schinnerer, E., Boone, F., et al. 2011, *A&A*, 529, 45
 van der Walt, S., Colbert, S. C., & Varoquaux, G. 2011, *CSE*, 13, 22
 Walter, F., Bolatto, A. D., Leroy, A. K., et al. 2017, *ApJ*, 835, 265
 Westmoquette, M. S., Smith, L. J., & Gallagher, J. S., III 2011, *MNRAS*, 414, 3719